CHARON/PLUTO MASS RATIO OBTAINED WITH HST CCD OBSERVATIONS IN 1991 AND 1993 [1]

G. W. Null and W. M. Owen, Jr.

Jet Propulsion Laboratory, California Institute of Technology, Pasadena, California 91109

ABSTRACT

We have analyzed *Hubble Space Telescope* wide field camera observations of Pluto, Charon, and a reference star, acquired in 1991 and 1993, to observe Pluto's barycentric motion and determine the Charon/Pluto mass ratio, $q = 0.1237 \pm 0.0081$, with 6.5% accuracy. Solution values for Charon orbital elements include the semimajor axis, $a = 19662 \pm 81$ km; inclination, $i = 96.57 \pm 0.24$ deg; eccentricity, $e = 0.0072 \pm 0.0067$; longitude of periapsis, $\varpi = 2 \pm 35$ deg; and mean longitude, $\lambda = 123.58 \pm 0.43$ deg. These elements are referred to the J2000 Earth equator and equinox at epoch JED 2446600.5.

[1] Based on observations with the NASA/ESA *Hubble Space Telescope*, obtained at the Space Telescope Science Institute, which is operated by the Association of Universities for Research in Astronomy, Inc., under NASA contract NAS5-26555.

1. INTRODUCTION

This article presents an observational solution for the Charon/Pluto mass ratio q, determined from *Hubble Space Telescope* (*HST*) observations of Pluto's barycentric motion. These measurements were acquired with quadrant WF1 of the first Wide Field Camera (WFC) CCD instrument. Two independent data sets, each spanning slightly more than 3 days, were acquired in August 1991 and August 1993. Mass ratio and Charon orbital element solutions obtained from the 1991 observations were reported in Null, Owen, & Synnott (1993; hereafter Paper 1) and some reader familiarity with that paper is assumed here.

The present work differs from Paper 1 in several important respects. First, the availability of the 1993 observations has enabled a good check between the two data sets and has significantly improved the mass-ratio solution. Second, improved field-distortion calibrations were possible both through acquisition of new WFC observations of star-field NGC1850 and through new reduction techniques which significantly increased the number of usable stars in each frame. This enabled higher order distortion solutions which revealed that the Paper 1 field distortion degree and order was too low. As discussed in Section 3.1, the resulting Paper 1 mass-ratio solution, $q = 0.0837 \pm 0.0147$, was flawed and should be replaced with our current results. Finally, NGC 1850 observations taken within a few days of each Pluto data set have provided an accurate solution for the WFC scale change between the two epochs; this provided important, *a priori* conditioning so that the combined 1991+1993 mass-ratio solution was relatively insensitive to field-distortion errors,

With all calibrations applied, mass-ratio solutions with the 1991 and 1993 data individually and the solution with the combined data are in good statistical agreement. The adopted mass-ratio solution based on the complete data set is $q = 0.1237 \pm 0.0081$, a 6.5% accuracy.

Young *et al.* (1994; hereafter Y94) obtained $q = 0.1566 \pm 0.0035$ from an analysis of six consecutive nights of observations at Mauna Kea observatory, our current solution clearly improves the agreement with this ground-based solution, but the results still differ by about 3.7 sigma. Possible speculative explanations can be found both in the ground-based and *HST* techniques. For example, the variation in the Y94 single-exposure mass-ratio solutions suggests that their standard errors (s.e.'s) may be too small by about a factor of two. Also, Y94 calibrated field distortion using relatively noisy observations of asteroid 1981 Midas, which could conceal errors as large as 0''.02. This could possibly cause errors as large as 0.02 in the mass ratio.

On the other hand, *HST* is a complicated system, and although we have carefully calibrated these *HST* data, have good agreement between the 1991 and 1993 mass-ratio solutions, and have a combined solution which appears to be relatively insensitive to known error sources, there is still a possibility of significant undetected systematic errors. We believe that a satisfactory explanation of the differences between the *HST* and ground-based results will require additional ground-based observations and that further discussion would not be very useful, Therefore, the remainder of this paper will discuss only our *HST* results.

Both the 1991 and 1993 observations were acquired prior to the Shuttle repair mission. However, as discussed in Paper 1, the degraded *HST* provides better CCD image sampling for the WFC but the repaired *HST* provides a smaller image point spread. Our current analysis suggests that comparable centroid accuracy is achievable with either configuration.

This article is divided into seven major sections. The observation program, data information content, and solution for uncalibrated image centroids are described in Sec. 2. Sec. 3 describes the calibration of these centroids. Sec. 4 presents our mass-ratio and Charon orbit solution, Sec. 5

examines the effect on the solution of varying the model assumptions, and Sec. 6 provides density solutions corresponding to some of the published Pluto and Charon radii, A summary and conclusions appear in Sec. 7.

2. OBSERVATION PROGRAM

2.1) *Observation Program Overview*

The 1993 observations were taken with the same observation modes (quadrant WF1, 4-sec exposure time, coarse guiding mode, filter F555W) as the 1991 observations. Paper 1 provides a more detailed description of the 1991 observations. As in 1991, three were seven *HST* visits in August 1993, with two exposures per visit. The reference star for the 1993 Pluto frames was GSC 5024/714, with peak central-pixel brightness of about 1000 DN.

Two calibration exposures of star cluster NGC 1850 *were* acquired to determine the distortion and scale stability between our 1991 and 1993 epochs. The two exposures were obtained at significantly different orientation angles, enabling an accurate determination of WF1 aspect ratio (between pixel scale and line scale) and geometric non-orthogonality. No additional faint-star exposures were acquired to monitor scale changes between Pluto visits because, as discussed in Paper 1, analysis of similar 1991 observations showed excellent inter-visit scale stability.

A detailed description of the 1993 exposures and the corresponding *HST* position and velocity coordinates is provided in Table 1. The Pluto and field distortion exposures are denoted as "PLUTO" and "GDCAL", respectively. We continue the visit numbering system introduced in Paper I. The *HST* coordinates were obtained from the *HST* Data Archive; they have an expected accuracy of about 200 m (GSFC 1987).

The Pluto-Charon observational geometry for the 1993 observations is shown in Fig. 1; locations of the Pluto exposures are shown as filled circles superimposed on the orbit. Paper I provides a comparable plot for the 1991 observations. Visits 8 and 9 are at the bottom of Fig. 1 and visits 10-14 are near the top; most of these visits are near maximum elongation. The 1993 observations covered the near side of Charon's orbit, not observed in 1991, and the orbit was much more! open in 1993 than in 1991. These differences in observation geometry significantly strengthened solutions containing both data sets.

As in 1991, the 1993 observations were acquired near the August low-angular-rate opportunity to maximize the Pluto-star observing span. Pluto's apparent motion relative to GSC 5024/714 is shown in Fig. 2. This geometry is similar to 1991's, except that Pluto appears on the west side of the star instead of the east side.

2.2) Mass-ratio Information Content

Paper I provides a detailed description of the mass-ratio information content for the 1991 observations, and that description applies to the 1993 data since the observing geometry is similar. Briefly, errors in Charon's coordinates contribute negligibly to tbe mass-ratio error and Pluto-star position angle information is removed by solving for the camera twist (orientation) angle on each visit. Thus, only observations of the Pluto-star angular distance (s_{p*}) have a significant effect on the mass-ratio solution.

Fig. 3 shows the changes in s_{p*} for perturbations of 0.01 in q and 1 part in 10^{-4} in scale. These perturbations are highly correlated during the 1991 observations but anticorrelated in 1993. There is a corresponding effect on mass-ratio solutions; a change in scale tends to induce equal and opposite changes in q for solutions with only 1991 or only 1993 data. For these solutions, the least-squares process compensates for other systematic errors (for example, field distortion errors) by making relatively large joint changes in scale and in q. This sensitivity is demonstrated in Sec. 5.2.

If the scale change between the 1991 and 1993 data sets can be highly constrained *a priori*, then the scales for the 1991 and 1993 data sets must move together when the data sets are combined. In that case, a scale change will produce a much smaller change in q, because the correlation between q and scale has been broken.

As will be discussed in Sec. 3.2, the NGC 1850 observations in 1991 and 1993 enabled the determination of an accurate value for the scale change between the 1991 and 1993 Pluto data sets. Also, as shown in Sec. 5.2, the sensitivity of q to systematic errors is significantly reduced when the scale-change constraint is imposed on the combined solution.

2.3) *Image Centroid Solutions*

The centroid solutions for the 1993 observations were obtained in exactly the same way as described in Paper I for the 1991 observations. WF1 point spread was represented by a sum of six Gaussian functions; the same Gaussian coefficients were used regardless of field position or epoch. Pluto and Charon centroids were obtained in simultaneous solutions. For both the 1991 and 1993 data sets, the raw centroid accuracy per exposure was usually about 0,020 to 0.025 pixels for Pluto and the reference star and about 0.07 to 0.08 pixels for Charon.

3. ASTROMETRIC CALIBRATIONS

Accurate image centroid calibrations are essential, because these calibrations are often larger than the errors in the random centroiding errors. This section describes the error sources and their calibrations, tabulates the calibrated centroid values, presents a summary of the raw centroids and their calibrations (Table 2), and constructs an image centroid error budget.

Two calibrations apply to all images: field distortion and the effects of scale changes. Albedo markings in Pluto can cause its centroid to shift relative to its center of mass. Proximity effects (image overlap) can cause systematic changes in Charon's centroid. Finally, the fact that Pluto presents a disk, not a point, may introduce a centroid shift. These calibrations are discussed in the following eight subsections: Field Distortion, Scale Change between 1991 and 1993, Pluto Albedo Variations, Pluto Uniform Disk, Pluto-Charon Overlap, Short-Term Scale Changes, Summary of Calibration Results, and Image-Centroid Error Budget.

3.1) *Field Distortion*

Distortion, defined here as the astrometric difference between the actual WFPC camera and the ideal gnomonic projection for a point source, was determined using the same techniques as in Paper 1. improvements to the process included using more frames and finding more stars per frame, so that more parameters could be included in the solution set. As before, the calibration target was LMC open cluster NGC 1850.

The five frames taken in August 1991 and analyzed in Paper I shared the same spacecraft roll angle. Consequently, as reported there, that data set did not yield any information on the size or shape of the pixels, since any linear deformation in the camera could not be distinguished from a systematic shift in the stars' positions. Paper I showed that reasonable changes to the pixel aspect ratio did not affect the mass ratio greatly, but it ignored a possible nonorthogonality between the pixel and line axes of the CCD chip.

In order to solve directly for both the aspect ratio and nonorthogonality, the two calibration frames requested in 1993 were taken with the spacecraft intentionally rolled in either direction from its nominal orientation by 20 degrees, the maximum possible under the flight rules. We also obtained seven more frames of NGC 1850 taken in 1990 and 1992, from the STScI archives.

The solution set includes the right ascension and declination of the optical axis and the camera twist angle for each frame, plus a separate scale for each different month of observation. The scale was assumed constant during each month; solving for separate scales for each exposure did not materially affect the results.

Aspect ratio was introduced by including in the solution set parameter b_{01}, which represents a change in the y coordinate proportional to y itself, Similarly, the nonorthogonality term was represented by parameter b_{10}, a change in y proportional to x. The two corresponding terms for x were omitted: a_{10} is subsumed by scale, and a_{01} by the twist angle. Likewise, a_{00} and b_{00} are replaced by the individual OTA right ascensions and declinations.

Our processing was also improved by the introduction of a different way of identifying stars. The former algorithm, described in Paper 1, merely divided each frame into 16 x 16 pixel regions, found the brightest pixel in each region, found the image centroid, and kept the result if certain statistical tests were passed. That algorithm detected an average of 630 stars in each frame. The new algorithm identified every local maximum brighter than 100 DN and then proceeded as before. Many more stars were found, of course, and the list was examined carefully to remove duplicate entries, saturated stars, close double stars, and '{side lobes" of bright stars, some of which passed the tests intended to discriminate against them. An average of 1000 stars on each frames survived this process, although not all win-e useful: stars that appear on only one frame do not contribute to the determination of distortion.

The large quantity of observations allowed us to extend the order of the Legendre polynomial fit. Whereas in our previous work the sixth-order terms were of marginal significance, now eighth-order terms could be determined with con fidence. Ninth-order terms were clearly meaningless, and their presence inflated the formal uncertainties on the other parameters as well. The eighth-order terms were very small and marginally significant. The scvellth-order terms, however, proved to be larger than anticipated; four had magnitudes of 0.1 pixels. We therefore retained all the scvcntll-order terms but deleted eighth-order terms in the adopted model.

Examination of the residuals revealed that four of the frames- two in September 1990 and two in July 1992-- had systematic trends in the corner near (O, 800). These four frames also exhibited the largest scale change, consistent with the published focus history of the OTA (Hasan & Burrows 1993). Evidently the distortion pattern depends somewhat on the separation between the primary and secondary mirrors. Since these four frames yielded discrepant results, and since their OTA focus was significantly different from that of the Pluto frames, we removed them from the data set.

The final solution, based on 6818 images of 1907 stars in the 10 retained frames, appears in Table 3. Our new solution is qualitatively similar to that in Paper 1. The four parameters associated with cubic Seidel distortion—a_{12}, a_{30}, b_{21}, and b_{03} - have changed by at most 0.11 pixels. Other low-order terms are in similar agreement. The aspect ratio coefficient b_{01} is quite small, but the chip dots exhibit nonorthogonality (b_{10}) at the ().1 -pixel level. Eight of the seventh-order terms were also of order 0.1 pixels.

The rms postfit residual was 0.042 pixels, and the reduction to unit weight was 1.18. These numbers are slightly higher than the corresponding results i n Paper 1, but this increase is caused by the higher percentage of fainter stars in the new fit. A solution using only the five frames from 1991 also gave higher residuals, comparable to those for the adopted solution. There was no detectable secular change in the distortion model, excepting of course for the four frames whose scale was so different from the others.

The corrections due to distortion to the observed centroids for Plute, Charon, and the field stars appear in Table 2. The formal sigmas on these c.corrections are never more than 0.007 pixels; even accounting for the adjustment to unit weight, the sigmas do not exceed 0.008 pixels. Trial solutions extending through higher orders or including all 14 calibration frames gave mapped corrections that differed from the adopted ones by at most a few hundredths of a pixel.

A comparison of these distortion corrections with those published in Paper I reveals significant differences, occasionally reaching 0.15 pixels. These differences are due primarily to the nonorthogonality and seventh-order terms, which were not included in our earlier work for reasons discussed ab ove.

One can also compare our distortion model with the sixth-order model developed by Gilmozzi *et al. (1994)* and implemented in the METRIC task in STScI's STSDAS software. An examination of the METRIC code shows that its goal is to reduce the four WF fields to a common scale and orientation, namely, that of quadrant WF2. It is unclear from the code whether aspect ratio and nonorthogonality are correctly accounted for. We found t hat, although M ETRIC's values for the most important coefficients were in good agreement with ours, the correction vectors differed by several tenths of a pixel, primarily due to differences in the "plate constant s." Agreement for the Pluto-star angular distance was much better: one visit had a difference of 0.13 pixels, four visits had differences between 0.05 and 0.08 pixels, ant] the other nine visits had differences less than 0.05 pixels. Angular distance residuals from the mass-ratio solution were slightly worse using the METRIC corrections than with our corrections.

We are confident that our adopted distention model represents fairly the astrometric behavior of the WF1 field for our purposes. Again we caution the reader that these results are based on centroids obtained from fitting with a symmetric point-spread function, and that other methods using asymmetric point spread functions or without a point spread function (for example, with a moment algorithm) may well produce subtly different results.

3.2) *Scale Change between 1991 and 1993*

In Paper 1, the scale (arcseconds per pixel) of quadrant WF1 was determined from the observed motion of Pluto's barycenter past the reference star. The same technique can be used with the second set of images to derive the scale in 1993. Section 5.2 snows that our ability to solve for the mass ratio is significantly enhanced if the change in scale from 1991 to 1993 can be determined independently.

A side benefit of the revised field distortion model is the determination of relative scales for the various sets of calibration frames. Our technique yields only relative scale changes, not absolute scales, because wc do not have accurate *a priori* catalog positions for the stars. We find a scale change of $+196 \pm 4$ parts per million (ppm) from August 1991 to August 1993. This value was remarkably stable: changing the order of tile Legendre fit or reintroducing the four discarded frames never changed the relative scale by more than half its formal error. By comparison, the deleted frames in 1990 and 1992 showed scale changes of 500 ppm relative to 1991.

These observed scale changes appear to be correlated with the published focus history (Hasan & Burrows 1993) of *HST*'s Optical Telescope Assembly (OTA). A plot of scale change against position of the OTA secondary mirror (Fig. 4) shows that five of the six epochs follow a linear relationship. The outlier will be discussed in detail Mow.

The cause of our observed scale changes- 26 ppm change per micron of OTA secondary motion- is not known. According to Burrows and Schroeder (private communication), motion of the OTA secondary should have a much smaller effect on the position of the chief ray, about 0.3 ppm per micron. We speculate that our centroids, which presumably track the center of light, must be exhibiting a different behavior from that of the chief ray.

Hasan & Burrows (1 993) also report OTA "breathing" in which the secondary mirror position changed by 2-5 microns over an *HST* orbit. Fig. 4 implies that breathing could produce scale changes of 50- 130 ppm. If we solve for separate scale changes for each frame rather than for each month, the frames for any month show variability of about 70 ppm within the month, in reasonable consistency with the changes expected from breathing.

The outlier in Fig. 4 was a solit ary frame, denoted GDCAL90-5 in Table 1, taken in November 1990 at an *HST* orbital longitude different from the other frames t aken in 1990. The for-ma] errors shown in Fig. 4 are much smaller than the 130 ppm errors which might be induced by OTA breathing. Also, Fig. 3 of Hasan & Burrows (1 993), from which the abscissas in Fig. 4 were taken, showed a few-micron scatter in secondary position relative to their best-fit line. Finally, since the field of the outlier had only a small overlap with the other frames, its scale is inherently *poorly* determined, to only 35 ppm.

Thus, the combined effects of these errors might account for much of the observed error for the November 1990 point. We have no other explanations for this outlier, but, in any case, this issue affects only the amount of correlation between scale change and OTA secondary motion, not the scale change between August 1991 and August 1993. Only the latter has any bearing on our determination of the Charon/Pluto mass ratio.

Despite the demonstrated correlation between OTA secondary motion and scale change, our observed scale change from 1991 to 1993 must be used with care. Recall that the distortion model forces one scale on all frames taken within a particular month. The small number of frames taken at each epoch (see Table 1) implies that some effects of breathing may remain in our monthly results,

Furthermore, in both August 1991 and August 1993 the frames of Pluto and of NGC 1850 were taken at different locations in the orbit, so OTA breathing may affect our assumption that a scale change derived from NGC 1850 can be applied directly to Pluto. However, there is some clustering of *HST* positions within the Pluto and NGC 1850 data sets, and this will probably reduce the maximum error. Also, the calibration frames in 1993 were taken three weeks after the Pluto frames, and in those three weeks the OTA secondary moved about half a micron (Hasan & Burrows 1993), presumably inducing a further scale change of 13 ppm. For these reasons we kept the scale change from 1991 to 1993 at 196 ppm, but we increased its uncertainty to 100 ppm.

3.3) *Pluto Albedo Variations*

Albedo models for our analysis were adopted from Buie & Tholen (1989) and Buie *et* al. (1992). Our current analysis used these models as described in Paper I. As in Paper 1, we adopted the Buie & Tholen (1989) "shelf" model for calibrations, but have also examined the solution sensitivity to other Buie & Tholen (1989) models as well as the tile model of Buie *et al.* (1992), The peak effect from the shelf model was about 200 km (0.1 pixels) and the rms effect was about 0.06 pixels. For the centroid error budget, we assumed the s.e. to be half of the rms effect.

3.4) *Pluto Uniform Disk*

When an asymmetric, irregular WF1 point spread function is convolved with a uniform disk representing Pluto, the resulting image has a different profile from that associated with a star. For the "shape-fit" centroid methods used in this paper, the changed image profile may produce a shifted centroid position. This raises questions about the validity of applying the field distortion calibrations (Sec 3.1) obtained from star images to calibrate the actual Pluto images.

To investigate these questions, WF1 images of Pluto, Charon, and stars were simulated using two different point-spread generation programs. The first program (Redding, Dumont & Yu 1993) applied a full ray trace model (hereafter denoted "COMP") to simulate WF1 images using optical system parameters obtained by Redding using prescription retrieval on WF1 star images. The second program was the Version 4.0 TINYTIM software package developed by Krist (1993, 1994); this software simulated images for WF1 based on mirror phase maps determined at STScI with PC6 star observations.

Simulated images were computed by COMP and TINYTIM at the (pixel, line) locations of each *HST* visit; pixel size was about 0.0036 arcsec. These images were convolved with a uniform Pluto disk of radius 0.063 arcsec and with a Gaussian function to represent *HST* pointing jitter. Assumed jitter s.e.'s were 0.03 arcsec for 1991 observations and 0.015 arcsec for 1993 observations; the smaller values used for 1993 reflect pointing improvements reported by Mo & Hanisch (1993), The convolved images were then rebinned into the actual WF1 pixel size and fit with our adopted "sum of Gaussian" centroid method.

As shown in 'J'able 4, the largest centroid shift for a single component of the Pluto centroid is --0.084 pixels, but the mean shift is in the range --0.024 to +0.036 pixels. A similar analysis for Charon found negligibly small centroid shifts for all visits.

For l'lute, there are significant biases in pixel and line for each year, which are related to the previously discussed differences in Pluto's image position on the CCD. However, these biases are absorbed by the right ascension and declination of the reference stars. The differences from the yearly means arc usually much smaller, with the notable exception of COMP's pixel shift for visit 13. The two models give results which differ by 0.091 pixels for visit 13; we have no explanation for this behavior.

There are other reasons for caution in interpreting these results. Examination ofthefar-field portions of the instrumental point spreads show very little correlation between the two models. Also, as discussed in the next sub-section, jnlagc-overlap analyses conducted with simulated star images gave centroid shifts which are a poor representation of the errors obtained with real star im ages. We have chosen not calibrate the real Pluto and ('haron centroids for the effect of Pluto's uniform disk, but will include this effect in the data error budget. As discussed in Sec 5.2, applying either COMP or TINYTIM centroid shifts from Table 4 has an essentially negligible effect on the mass-ratio solution.

3.5) *Pluto-Charon Image Overlap*

For this analysis, we used image registration techniques as described in Paper 1, with minor differences disc. ussed below. The earlier analysis was based on registration of star images taken from WF1 observations of N GC188. By systematically varying the registered positions of two images by increments of one pixel, it was possible to investigate the effect of image overlap for cases in which the non-overlapped position could be accurately determined.

Centroid determinations with the overlapped images gave a significant centroid shift of as much as 0.09 pixels in the radial direction. This shift could be roughly calibrated as a function of angular distance, but a significant calibration could not be determined for the tangential component. The noise for eat}] angular distance calibration was roughly half the size of t he calibration.

The present analysis is much more extensive, with image registration results for both simulated images and real images. We first attempted to obtain suitable centroid calibrations by using simulated Pluto and Charon WF1 images. Centroid shifts vs. angular distance showed significantly more noise for these images than for comparable star images; this noise is probably associated with the broadening of the Pluto image. A comparison of image-overlap results with simulated WF1 star images and image-overlap results with real WF1 star images showed very poor agreement, and so neither COMP or TINYTIM appears to be suitable for determining the centroid shift induced by overlap between Pluto and Charon. Also, overlap results from the two simulation programs were not in good agreement. These results led us to conclude that these simulated images are not suit able for an image overlap analysis.

Our adopted method was to register actual Pluto WF1 images with actual star images chosen to have about the same pixel brightness as the actual Charon image. If necessary, an additional brightness scaling was performed. Several stars were used, and all gave essentially the same overlap centroid results. For each visit, centroid shifts in terms of angular distance (AS) and tangential component ($S\Delta P$) were obtained for all possible separations in pixel and line, except that a small region about the real Char on images was excluded. This process was repeated for all 14 visits and the results were merged and sorted into angular distance bins.

Our results are shown in Table 5. The first column contains the angular distance for the bin center, and the second column displays the corresponding mean AS. The next two columns display s.e.'s, computed about the mean for AS and about zero for $S\Delta P$. The fifth column provides the number of different registrations, and the last colu Inn gives the difference between the calibrations obtained for Paper 1 and those for the present paper.

The peak angular distance shift is 0.089 pixels, nearly the same as for Paper I, but the results differ by about 0.05 pixels in many of the bins. The s.e. about the mean is usually slightly larger that for Paper 1, probably because the present work had a broader Pluto image and used Pluto images from 14 different WF1 positions. The raw Charon centroids were calibrated with image-overlap shifts from interpolated from the second column of 'l'able 5 and projected into pixel and line. By a similar process, the tabulated s.e.'s arc included in the error budget for each visit.

3.6) *Short-Term Scale Changes*

As part of tile 1991 observing program, WF1 exposures of a few fa int background stars were acquired within a fcw hours of each Pluto visit in order to examine short-term changes in scale. Analysis of those exposures, described in Paper I, showed an rms scale. change of about 4 parts in 105, roughly the same as the forma] se. for each visit. We concluded that there were no significant scale variations between the 7 visits.

Scale exposures were not requested for the 1993 data set because the 1991 results appear to provide adequate assurance of scale stability. We therefoı c do not calibrate for inter-visit scale changes. Scale changes may make a (),03 pixel error contribution for the largest Pluto-star angular distances. We did not include this error source in the error budget.

3.7) *Summary of Calibration Results*

Three calibration corrections were applied as shown in Table 2: 1) Pluto, Charon, and the reference star centroids were calibrated for field distortion; 2) Pluto centroids were calibrated for albedo variations, as obtained from the "shelf" model of Tholen & Buie (1 989); and 3) Charon centroids were calibrated for image overlap.

A significant scale change between 1991 and 1993 was determined as a by-product of the field distortion solutions; the scale-change value and s.e. were used as *a priori* conditioning for the mass-ratio solutions. Visit-to-visit scale changes within each year were insignificant, so no corrections were applied. We were able to bound the possible effect of Pluto's finite disk but could not obtain suitable calibrations.

3.8) *Image Centroid Error Budget*

In Paper 1, we obtained mass-ratio solution s.e.'s adjusted to unit weight, but, in retrospect, we see that this procedure resulted in a mass-ratio se. which was about three times smaller than the actual error. Unit weight adjustments are inherently flawed, because they do not reflect errors which have been absorbed into the solution parameters.

For the present analysis, we have instead constructed an observation error budget for usc in data weighting, As discussed in Sec. 4.3, these data weights result in a mass-solution χ^2 statistic which is significantly less than unity. 'l'able 6 shows the observation error budget expressed as formal s.e.'s on a per-visit basis, This table displays only those contributions which do not change from visit to visit. The image-overlap contribution (not shown in Table 6) is computed by interpolation of '1'able 5 to the Pluto-Charon angular separation s_{PC} for each visit.

The 'J'able 6 error budget was obtained under the following assumptions. For raw centroids, the per-visit values are obtained by dividing the per-exposure values by $\sqrt{2}$. The field distortion contingency was included to represent possible field distortion systematic errors which arc not reflected in the field distortion covariance. The s.e. for the albedo-variation error source (already stated in Sec 3.3) was assumed to be half of the rms of the adopted "shelf" model calibration. The Pluto finite disk contribution was was computed as the average of the rms centroid shifts computed with the TIN YT1M and Co M}' methods.

For Pluto and the reference star, the total error contribution per visit is 0.056 and 0.026 pixels, respectively, and the pcr-exposure value is greater by a factor of $\sqrt{2}$. For Charon, the *a priori* s.e.'s were obtained for each visit from a statistical combination of error budget and image overlap s.e.'s. The per-exposure s.e.'s for Charon range from 0.126 to 0.263 pixels, depending on the angular separation between Pluto and Charon.

4. SOLUTION FOR MASS RATIO AND CHARON ORBITAL ELEMENTS

The solution method was identical to that employed for Paper I. All ephemeris coordinates and elements were referred to the mean Earth equator and equinox of J 2000. Planetary ephemeris coordinates were obtained from JPL Development Ephemeris DE202 (Standish 1990), and the conic elements for Charon were obtained from Tholen & Buie (1990; hereafter TB90). Simultaneous least-squares solutions were performed for the parameters defined in the next subsection. Each solution converged completely within four iterations.

4.1) Definition of Solution Parameters and A priori Standard Errors

Solution parameters included the Charon/Pluto mass ratio $q = \mathcal{M}_C/\mathcal{M}_P$, right ascension and declination for each of the two reference stars, and seven Charon equinoctial elements [a, $e\sin(\omega+\Omega)$, $e\cos(\omega+\Omega)$, $\lambda = M_0 + w + \Omega$, $\tan\frac{1}{2}i\sin\Omega$, $\tan\frac{1}{2}i\cos\Omega$, $1/P$], where P = Charon period in days. Other parameters included S_{91} and S_{93}, the WF1 scales in 1991 and 1993 in units of arcsec/pixel.

Also, for each of the 28 exposures, there were three solution parameters specifying the right ascension α_j, declination δ_j, and twist angle κ_j of the WF1 CCD quadrant; here j is the exposure index. These parameters adjust the inertial position and orientation of the WF1 quadrant to the observed position of Pluto and the reference star. The angular reference for this solution is provided by the well-known angular motion of the Pluto barycenter; this enables an accurate orientation of the periodic barycentric motion and of the Charon orbital elements (especially the inclination i). *A priori* s.e.'s were 1 deg for all these angular variables, but we were able to obtain solution s.e.'s of 0.005 to 0.016 arcsec for α_j and δ_j and 0.007 to 0.014 deg for κ_j.

We used essentially infinite *a priori* standard errors for most parameters. However, more restrictive assumptions were used for two solution parameters, namely Ω and P. The *a priori* value and s.e. for Charon's period (P = 6.387246 ± 0.000011 days) were taken from TB90. Since the TB90 Charon node solution Ω = 223.015 ± 0.028 deg is about 16 times more accurate than the unconstrained solution provided by our data, the TB90 solution for Ω was transformed into correlated *a priori* information for our solution parameters $\tan\frac{1}{2}i\sin\Omega$ and $\tan\frac{1}{2}i\cos\Omega$, using a 100-deg uncertainty in orbit inclination.

For Paper I, it was not possible to provide an accurate calibration of the pixel aspect ratio, there denoted as S_y/S_x. However, we now have an very accurate calibration from the field distortion solution, namely 1.000044 ± 0.000012, well below the error level which causes significant changes to our solutions. Therefore, we have not included the aspect ratio as a solution parameter.

For our combined solution, *a priori* conditioning of the scale change between the 1991 and 1993 observation epochs was obtained from the field distortion analysis as described in Sec 3.2. The *a priori* value and se. for the scale change from August 1991 to August 1993 were 0.000020 ± 0.000010 arcsec/pixel.

4.2) Solution Results

All the solution parameter s.e's presented for the present analysis are formal errors, based on data weights computed as described in Sec. 3.8. Since these data weights represented our best estimate of the actual errors, no unit weight adjustments were made.

Table 7 presents our solutions with the 1991, 1993, and combined data sets, and our published Paper I solution. No values are shown for Ω and P, since these parameters had strong a *priori* conditioning and the solution values were well within the *a priori* s.e. 's. Solution values Of α_j, δ_j, and κ_j are not tabulated, since this information is not useful for most readers. The adopted value for q *is* larger than the values obtained from the 1991-only and 1993-only solutions because the scale-difference *a priori* conditioned the combined solution for q, but did not affect the single-year solutions.

There are two significant differences between the Paper 1 solution and our current 1991-only solution, both due to calibration improvements described in Sec. 3. First, the change in a is caused by our adoption of a more accurate image-overlap calibration; second, the change in the mass ratio was caused by more accurate calibration of field distortion. The solutions presented in Table 7 have excellent consistency, well within the quoted errors. We adopt the combined solution as our final result.

Table 8 compares our adopted solution with those obtained from ground-based observations by Y94 and TB90. Our adopted mass-ratio solution agrees much better with Y94 than did our Paper I solution, but there is still a significant difference between these solutions. Our new solution for a agrees well with TB90, but less well with Y94. Finally, there is about a 4.6 sigma difference between the inclination from Y94 and our own result. Recent *HST* Planetary Camera observations of Pluto and Charon by Tholen, Buie, & Wasserman (1994) may eventually provide much more accurate solutions for the Charon orbital elements then those discussed here.

4.3) *Observation Residuals for the Adopted Solution*

The observation residuals in pixel and line, the corresponding *a priori* s.e.'s, and the mean and s.e.'s for each body arc shown in Table 9. The s.e.'s (pixel and line combined) were 0.025, 0.056, and 0.006 pixels for Pluto, Charon, and reference stars, respectively. This compares reasonably well with the corresponding results from Paper I (0.017, 0,061, 0.014 for Pluto, Charon, and star).

Residuals and *a priori* s.e.'s for the Pluto-star angular distance s_{P*} arc displayed in Table 10. As discussed in Sec 2.2, s_{P*} provides essentially all the information for the mass-ratio solution. The overall s.e. for s_{P*} is 0.039 pixels, slightly smaller than the Paper 1 value of 0.043 pixels. For the present work, the weighted se, is 0.466. A unit weight adjustment based on 28 exposures and six essentially unconstrained solution parameters (q, right ascension and declination for each reference star, and a single scale parameter) can be obtained by multiplying 0.466 by 1.13. The resulting statistic $\sqrt{\chi^2_\nu}$ is 0.526, indicating that the *a priori* data s.e.'s are about a factor of two larger than that required for unit weighting. As discussed in Sec. 3.8, we chose not to apply a unit weight adjustment, but instead computed *a priori* data s.e.'s from the error budget. All mass-solution s.e's in this article are therefore estimates of both the formal error and the actual error.

5. SENSITIVITY ANALYSIS

It is useful to examine variant solutions, in which changes are made in the data set, data calibrations, or a *priori* assumptions. This can provide valuable information about the sensitivity of the solution parameters to possible random and systematic. errors.

5.1) *Sensitivity to Data Deletions*

The combined solution was very resistant to data deletions. Solutions were performed to examine the effect of removing the data for each of the 14 visits. Other solutions used only the first exposure or second exposure from each visit. Expressed in multiples of the adopted solution s.e., the largest deviation for mass ratio, semimajor axis, eccentricity, apse, or inclination was 0.75 s.e. and most deviations were much smaller. This stability is much better the 1991-only stability described in Paper I, primarily because the present analysis could use a much larger data set with only a small increase in the. number of solution parameters.

5.2) *Sensitivity to Calibration Model Assumptions*

The sensitivity of q to systematic errors is presented in Table 11. As can be seen, q is relatively sensitive to systematic errors in the 1991 -only and 1993-only solutions, but is much less sensitive in the combined solution, For field distortion solutions of degree and order 3 or more, the combined solution for q is within one s.e. of the adopted solution. Other effects, such as Pluto's uniform disk and albedo model, produce changes in q of a few tenths of an se. Removal of the *a priori* information for scale difference also causes a very small change in q. For this case, the solution s.e. for q (not shown in Table 11) increases by about a factor of two. A sensitivity analysis (also not shown in Table 11) showed that q decreases by approximately 0.00470 when the scale difference increases by 10^{-5} arcsec/pixel.

The statistical model for our solutions assumes that the observed data have Gaussian errors and that all systematic errors can be represented using known functional forms. Of course, many of the systematic calibration errors have poorly known functional forms and often only approximate magnitudes are available. We have attempted to obtain a valid error description by adopting the err-or budget of Sec 3.8, which increases the *a priori* data s.e.'s to include our rough estimates of the systematic error magnitudes. This process may be optimistic or pessimistic, depending on the actual unknown profile of each systematic error and so the results in Table 11 provide a necessary, but not completely conclusive, confirmation of solution strength and stability.

For a more conservative analysis, assume that the perturbation profile in s_{P*} is perfectly correlated with the profile of $\partial s_{P*}/\partial q$. From Fig. 3, a worst-case error profile with peak error of 0.1 pixel would cause errors in q of about 0.02. However, from the analysis of Sec. 3, there appears to be a low probability of having an uncalibrated perturbation which is 0.1-pixel or larger and which closely mimics the worst-case profile. Thus, we conclude that the adopted solution s.e.'s remain the most suitable description of the real errors.

Table 12 shows the sensitivity of Charon's orbital elements to the most important systematic. error sources. These effects are mostly at the level of a few tenths of a solution se.

5.3) *Sensitivity to Charon Orbit Element Assumptions*

Table 13 compares our adopted solution to three variant solutions, The solutions for inclination and semimajor axis are very insensitive to these assumptions, but removal of the node a *priori* information dots cause a significant increase in the longitude uncertainty. Removal of all *a priori* constraints causes an even larger increase in longitude uncertainty and a small increase in eccentricity uncertainty. We chose to solve for eccentricity in our adopted solution, since this does not have a significant, effect on the other solution parameters or s.e.'s. Node and period *a priori* s.e.'s from TB90 were adopted to provide increased solution strength in eccentricity and longitude.

Finally, the values of q from the variant solutions differed from the adopted solution by less than 0.02 s.e., and the s.e's were negligibly different. As in Paper 1, this confirms that the solution for q is not sensitive to the Charon observations.

6. PLUTO AND CHARON MASSES AND DENSITIES

This section presents the computed values and s.e.'s for the masses, gravitational constants, and densities of Pluto and Charon. As in Paper 1, density values are computed from our adopted solution (Table 7) combined with radius solutions from the literature. Also, sufficient information is provided to enable calculation of density values and s.e.'s when improved radius solutions are available.

6.1) *Parameter Values and Uncertainties for Mass and Density Calculations*

Table 7 gives parameter values and uncertainties which will be used to compute the derived masses and densities. For readers who wish to combine our mass solution with new solutions for the radii, the covariance matrix Γ for solution parameters a, P, and q has elements: $\Gamma_{aa} =$ 6575.5950, $\Gamma_{PP} = 1.2023646 \times 10^{-10}$, Γ_{qq} = 6.5250832 x10-5, $\Gamma_{aP} = -3.1621269 \times 10^{-6}$, Γ_{aq} = 0.052492423, and $\Gamma_{Pq} = -7.0076266 \times 10^{-11}$. We used this matrix to compute the mass and density s.e.'s. The solution value for Charon period (not given in Table 7 because it was strongly constrained by *a priori* from TB90) was $P =$ 6.3872473 deg/day.

6.2) *Masses and Gravitational Constants*

The masses and gravitational constants of Pluto, Charon, and the Pluto system computed from our adopted mass solution (Table 7) are shown in Table 14. Calculation of masses was based on the 1976 IAU value for the universal gravitational constant. The system mass is $\mathcal{M}_{\mathbf{sys}}$ = (1 .35+ 0.019)x 10^{s} inverse solar masses, agreeing exactly with the solution value of Beletic *et al.* (1 989), but about three times more accurate.

6.3) *Computed Density for Pluto and Charon*

Paper 1 describes available radius solutions through the end of 1992. Since then, Young & Binzel (1 994; hereafter YB94) have obtained Pluto and Char on radius solutions, with mutual event observations which are independent of those used by TB90, using solution techniques designed to be relatively insensitive to limb profiles and albedo distributions. Their radii were determined in units of Charon's semimajor axis; we display these radii referred to $a = 19640$ km for easy comparison to the TB90 values and denote them by $\tilde{R}_P$ and $\tilde{R}_C$ for Pluto and Charon, respectively. The resulting radii are $\tilde{R}_P = 1176 \pm 6$ km and $\tilde{R}_C =$ 628 ± 16 km. The absolute radii are then computed from $R_P = \tilde{R}_P(a/19640km)$ and $R_C = \tilde{R}_C(a/19640km)$.

Albrecht *et al.* (1994; hereafter A94) analyzed *HST* FOC observations of Pluto and Charon and obtained solutions of Rp==1160 km and R_C=650 km with filter F550M and $R_P = 1160$ km and $R_C =$ 635 km with filter F342W. Because these solutions are preliminary, no error bars were provided.

Table 15 shows a representative set of radius solutions as well as the density values and s.e.'s obtained by combining this information with our adopted solution, Besides the previously discussed radius solutions, there are also entries for Elliot & Young (1 991; hereafter EY91) and Elliot & Young (1992; hereafter EY92). As can be seen, many of the radius and density solutions are in relatively poor agreement. Pluto's density ρ_P ranges from 1.79 to 2.05 g/cm^3 and Charon's density ρ_C ranges from 1.41 to 1,85 g/cm3. The solution s.e.'s for ρ_P are 0.03 to 0.05 g/cm^3 and for ρ_C are 0.]5 to 0.16 g/cm^3; these s.e.'s are much smaller than the solution range.

These results suggest that Charon may have a smaller density than Pluto, although the TB90 solution is marginally consistent with equal densities. However, the scatter in the current solutions for Pluto and Charon radii makes it difficult to reach any definitive conclusions about the densities.

If we use Y94's value in place of our own and then compute densities based on the 'TB90 radii, then ρ_P decreases by about 0.06 g/cm^3 and ρ_C increases by about 0.44 g/cm^3. Therefore, until the difference between our mass-ratio solution and that of Y94 is resolved, both radius and mass errors potentially have a significant, effect on the value of ρ_C. On the other hand, ρ_P appears to be limited primarily by radius errors.

The Pluto system density for TB90 and YB94 depends only on the radius solutions; these densities in g/cm^3 are 2,03 $\pm$ 0.03 and 1.88 $\pm$ 0.03, respectively. System densities with the A94 radii are approximately 1.90- 1.95, and have a weak dependence on our solution for a.

7. SUMMARY AND CONCLUSIONS

We have presented a new solution for the Charon/Pluto mass ratio q and Charon orbital elements, based on a combination of two independent WFC data sets acquired in 1991 and 1993. Solution values include the mass ratio, g = 0.12373: 0.0081; semimajor axis, a = 19662 ± 81 km; inclination, i = 96.57 ± 0.24 deg; eccentricity, e = 0.00723 0.0067; longitude of periapsis m = 2 ± 35 deg; and mean longitude, λ = 123.58 ± 0.43 deg at JED 2446600.5. The adopted solutions for q and a supersede that in Paper 1, which used only 1991 observations and was flawed by inadequate calibrations for field distortion and image overlap.

Solution para.meters for the adopted solution were shown to be relatively insensitive to known error sources, primarily because the combined data set provided twice the number of data available for Paper 1, with only a small increase in the number of solution parameters. Also, the field distortion analysis of NGC 1850 observations provided an excellent *a priori* solution for the scale change between the two Pluto data sets, which further constrained and improved the adopted solution for q. The mass-ratio solution stability was also demonstrated by good agreement between solutions performed with 1991 and 1993 Pluto observations. Solutions with only 1991 data and only 1993 data gave g = 0.1158 ± 0.0227 and q = 0.1204 ± 0.0319, respectively, and were consistent with the combined solution.

We have computed bulk densities based on our mass solution and representative radius solutions from the literature. Differences in the radius solutions produced a range of density values (Table 15) from 1.79 to 2.05 g/cm^3 for Pluto and and from 1.41 to 1.85 g/cm^3 for Charon. Table 15 suggests that Charon's density may be less than Pluto's. On the other hand, the Y94 mass-ratio solution yields a density for Charon about 0.44 g/cm^3 higher than our own values. Obviously, more observations and analysis are needed to improve and verify the accuracy of both the radius and mass determinations. In any case, a spacecraft mission to Pluto will probably provide very accurate values for masses, radii, and densities within the next 10 to *20* years.

The authors thank J). C. Redding of JPL for providing simulated COMP images, C. J. Burrows of STScI and D. J, Schroeder of Beloit College for information about OTA performance, A. Storrs of STScI for assistance with GO4292 sequencing, and D. G. Monet (USNO Flagstaff Station) and D. J. Tholen (Institute for Astronomy, Honolulu) for helpful discussions.

The research described in this paper was carried out by the Jet Propulsion laboratory, California Institute of Technology. This work was supported by NASA through grant number GO-4292.01-92A from the Space Telescope Science institute, which is operated by AURA, Inc., under NASA contract NAS 5-26555.

REFERENCES

Albrecht, R., *et* al. 1994, ApJ, 435, L75 (A94)

Beletic, J. W., Goody, R. M., & Tholen, D.J. 1989, Icarus, 79, 38

Buie, M. W. & Tholen, D. J. 1989, Icarus, 79, 23

Buie, M. W., Tholen, D. J., & Horne, K. 1992, Icarus, 97, 211

Elliot, J. L. & Young, L. A. 1991, Icarus, 89, 244 (EY91)

Elliot, J. L. & Young, L. A. 1992, AJ, 103,991 (EY92)

Gilmozzi, R., Kinney, E. K., Ewald, S. P., Panagia, N., & Romaniello, M. 1994, ApJ, 435, L43

Goddard Space Flight Center 1987, Science Scheduling to Mission Scheduling interface Control Document, Rev. E, Space Telescope document S'1'- ICD-11 E (GFSC, Greenbelt)

Hasan, 11. & Burrows, C. J. 1993, in *Calibrating Hubble Space Telescope*, Proceeding of Workshop Held at the Space Telescope Science Institute (Nov. 15-17, 1993, J. C. Blades and S. J. Osmer, eds.), 395

Krist, J, 1 993, in *A stronomical Data Analysis Software and Systems 11*, AS}' Conference Series 52, R.J. Hanisch *et* al., eds., 530

Krist, J. 1994, The Tiny Tim User's Manual, Version 4.0

Mo, J. & Hanisch, 11.1993, in *Newsletter of STScI's Image Restoration Project*, Summer 1993, No. 1, B. Hanisch, cd., 66

Null, G. W., Owen Jr., W. M. & Synnott, S. 1'.1993, AJ, 105, 2319 (Paper 1)

Redding, D., Dumont, 1'., & Yu, J. 1993, Applied Optics, 32, 1728

Standish, E. M., Jr. 1990, A&A, 233, 272

Tholen, D. J. & Buie, M. W. 1990, HAAS, 22, 1129 ('1']190)

Tholen, D. J., Buie, M. W., & Wasserman, I,. }1. 1994, BAAS, 26, 1554

Young, E. F. & Binzel, R. P. 1994, Icarus, 108, 219 (YB94)

Young, L. A., Olkin, C. B., Elliot, J. 1,., Tholen, D. J., & Buie, M. W. 1994, Icarus, 108, 186 (Y94)

Figure Captions

FIG. 1. The apparent orbit of Charon relative to Pluto, oriented relative to the WF1 field for exposures 8-13. Dots mark the observed offsets; visit 8 is at the lower right.

FIG. 2. The path of the Pluto/Charon barycenter past star GSC 5024/714 in 1993, with individual visits marked. The wiggles are caused by parallax due to *HST*'s orbital motion. Fields of view for the first and last visit are indicated; the last visit was rotated relative to the other six. *HST*'s optical axis lies near the westernmost corner for visits 8-13 and near the southwest corner for visit 14. Inset: the apparent orbit of Char on relative to Pluto in 1993; the square measures 2" on a side.

FIG. 3. The sensitivity of the observed separation between images of Pluto and the reference star to a change in telescope scale of one part in 104 (circles) and to a change in the Charon/Pluto mass ratio of 0.01 (triangles).

FIG. 4. The observed scale change in quadrant WF1 for exposures of NGC 1850, relative to the scale in August 1991, plotted against the modeled position of the OTA secondary mirror (Hasan & Burrows 1993). The scale for the November 990 exposure was poorly determined because its field had very little overlap with the other fields.

TABLE 1. Geometric properties of exposures other than those listed in TABLE 1 of Paper]. Quantities are tabulated for the midpoint of each exposure; vectors are geocentric and referred to J2000 coordinates.

TABLE 2. Observed image centroids and corrections to them. The first coordinate is in the pixel (column) direction; the second is in the line (row) direction.

TABLE 3. Coefficients of the adopted field distortion model. The a_{ij} and b_{ij} are measured in pixels. Uncertainties, in parentheses, are standard errors expressed in units of the fourth decimal.

TABLE 4. Centroid shifts due to the finite disk of Pluto, obtained for each visit using the programs COMP and TINYTIM.

TABLE 5. Centroid shifts for Charon due to image overlap with Pluto, binned by the separation between the two images.

TABLE 6. The adopted standard error for images of Plute, Charon, and the reference stars.

TABLE 7. The adopted solution from this paper compared to solutions using only 1991 or 1993 data and to the solution presented in Paper 1. Uncertainties, in parentheses, arc in units of the final digit for each parameter.

TABLE 8. The adopted solution from this paper compared to solutions by Young *et al. (1994)* and Tholen & Buie (1 990). Uncertainties, in parentheses, are in units of the final digit for each parameter.

TABLE 9. Postfit residuals, in pixels, and weighted postfit residuals for images of Pluto, Charon, and the reference stars. The adopted standard error for Charon images is also tabulated; the standard error for all images of Pluto and the reference stars was 0.076 and 0,037 pixel, respectively, as shown in TABLE 6.

TABLE 10. Predicted separation in pixels between images of Pluto and the reference star in each exposure, with postfit residuals and weighted post fit residuals for the same. The standard error in the separation was 0.085 pixel for each exposure,

TABLE 11. Sensitivity of the mass ratio q to changes in the various calibration models. The rightmost column gives the RSS residual of the separation between images of Pluto and the reference star.

TABLE 12. Sensitivity of Charon's orbital elements to changes in the various calibration models, expressed as fractions of the formal error of the adopted solution.

TABLE 13. Sensitivity of Charon's orbital elements to *a priori* constraints on them. Uncertainties, in parentheses, are in units of the final digit for each parameter.

TABLE 14. Masses and gravitational constants derived from the solution parameters in TABLE 7. Uncertainties, in parentheses, are in units of the final digit for each parameter.

TABLE 15. Computed densities of Pluto and Charon based on the masses from TABLE 14 and radii from the literature. Uncertainties, in parentheses, are in units of the final digit for each parameter.

TABLE 1. Geometric properties of exposures other than those listed in TABLE 1 of Paper I. Quantities are tabulated for the midpoint of each exposure; vectors arc geocentric and referred to J2000 coordinates.

Exposure	STScI Rootname	Exposure Time (UTC)	HST Position (km)			HST Velocity (km/s)		
			x	Y	2	x	Y	z
PLUTO8A	w1i40101t	1993 Aug 04 15:32:18.465	-5058.9	–3508.5	3250.2	3.9882	-6.3970	–0.7029
PLUTO8B	w1i40102t	1993 Aug 04 15:38:18.465	–3277.1	–5487.8	2757.2	5.7840	–4.4587	–2.0008
PLUTO9A	w1i40201t	1993 Aug 04 23:34:18.465	-5044.2	–3555.7	3221.3	3.9688	–6.3'319	--0.8453
PLUTO9B	w1i40202t	1993 Aug 04 23:40:18.465	– 3270.3	–5529.7	2680.5	5.7602	–4.4344	–2.1204
1'I,LJI'O1OA	w1i40301t	1993 Aug 0601:20:18.466	-4039.2	–4968.3	2'732.4	5.0682	—5.2422	--2.0402
PI ,UTO10B	w1i40302t	1993 Aug 06 01:26:18.466	--)'355.4	–6432.0	1809.3	6.3602	--2.7851	–3.0219
PLUTO1 1A	w1i40401t	1993 Aug 0614:08:18.467	–4912.3	–3937.1	2973.7	4.0191	–6.2151	–1.5919
PLUTO11B	w1i40402t	1993 Aug 0614:14:18.467	-3130.8	–5820.3	2189.7	5.7518	–4.1130	–2.7073
PLUTO12A	w1i40501t	1993 Aug 07 06:12:18.467	-4914.8	–4028.2	2845.3	3.9845	–6.1662	–1.8484
PLUTO12B	w1i40502t	1993 Aug 07 06:18:18.467	--3145.2	–5887.3	1981.0	5.720'3	–4.0301	–2.8911
PLUTO13A	w1i40601t	1993 Aug 0712:37:18.467	–5056.9	–3840.0	2857.0	3.7605	–6.3109	–1.8278
PLUTO13B	w1i40602t	1993 Aug 0712:43:18.467	–3355.2	–5764.1	1999.2	5.5726	–4.2421	–2.87(37
PLUTO14A	w1i40701t	1993 Aug 0717:26:18.468	–5104.7	–3791.2	2837.4	3.6799	–6.3480	–1.8627
PLUTO14B	w1i40702t	1993 Aug 0717:32:18.468	–3427.7	–5732.1	1968.8	5.5178	–4.2966	–2.9009
GDCAL90- 1	w0bs0104t	1990 Aug 1701:00:04.426	5253.7	4615.6	83.0	–4.3427	,5.0)84	–3.6045
GDCAL90- 2	w0bs0204t	1990 Aug 17 23:36:04.427	5512.8	4302.1	92.6	–4.1151	5.2072	--3.6041
GDCAL90 3	w0bs6104t	1990 Sep 20 07:06:04.462	4885.8	4470.5	2215.1	–5.3982	4.5621	2.6895
GDCAL90 4	w0bs6204t	1990 Sep 20 11:56:04.462	50'32.0	4262.7	2159.6	–5.1740	4.7851	2.7422
GDCAL90- 5	w0bs8104t	1990 Nov 29 19:17:04.456	2377.3	6372.0	1602.5	–6.1275	3.0907	--3.1639
GDCAL92- 1	w10i0101t	1992 Jul 20 23:58:46.645	6667.6	1227.0	- 1635.4	–0.4955	6.8622	3.1367
GDCAL92- 2	w10i0102t	1992 Jul 21 00:13:46.644	3355.6	5927.2	147'9.9	–6.2721	2.7377	3.2257
GDCAL93- 1	w1i40901t	1993 Aug 28 22:23:46.610	–5606.8	4098.4	–550.6	–3.7140	–5.5481	–3.5629
GDCAL93- 2	w1i40801t	1993 Aug 2919:15:46.612	-5288.3	4489.2	–643.2	–4.0769	—5.2997	–3.5447

TABLE 2. Observed image centroids and corrections to them. The first coordinate is in the pixel (column) direction; the second is in the line (row) direction.

	PLUTO1A	PLUTO1B	PLUTO2A	PLUTO2B	PLUTO3A
Pluto raw centroid	405.024, 160.491	403.249, 161.151	318.713, 199.431	347.191, 200.235	216.680, 410.520
Distortion correction	−0.153, 0.782	−0.146, 0.788	0.133, 0.909	0.142, 0.909	0.603, −0.047
Albedo correction	−0.048, −0.040	-0.048, --0.040	--0.047, −0.035	--0.047, −0.035	−0.093, 0.027
Pluto net Observable	405.225, 159.749	403.443, 160.403	348.627, 198..557	347.096, 199.361	216.170, 410.540
Charon raw centroid	401.624, 167.805	399.783, 168.574	345.834, 204.847	344.255, 205.561	217.663, 405.870
Distortion correction	−0.140, 0.807	−0.132, 0.813	0.154, 0.902	0.164, 0.902	0.604, −0.031
Overlap correction	0.007, −0.014	0.007, --0.014	--0.034, 0.063	--0.035, 0.063	0.014, −0.067
Charon net observable	401.757, 167.012	399.908, 167.775	345.714, 203.882	344.126, 204.596	217.045, 405.968
Star raw centroid	491.323, 698.200	491.093, 698.260	492.524, 604.286	492.477, 604.396	528.913, 381.623
Distortion correction	−0.183, −0.365	−0.183, --0.365	.-0.327, −0.589	--0.327, −0.589	−0.703, 0.068
Star net observable	491.506, 698.565	491.276, 698.625	492.851, 604.875	492.804, 604.985	529.616, 381.555

	PLUTO3B	PLUTO4A	PLUTO4B	PLUTO5A	PLUTO5B
Pluto raw centroid	215.542, 411.170	152.921, 556.487	150.915, 556.871	153.348, 643.399	151.677, 643.611-
Distortion correction	0.605, −0.049	0.594, --0.418	0.592, −0.414	0.264, −0.369	0.257, −0.361
Albedo correction	−0.093, 0.027	−0.095, 0.001	.-0.095, 0.001	--0.081, −0.034	−0.081, −0.034
Pluto net observable	215.030, 411.192	152.422, 556.904	150.418, 557.284	153.165, 643.802	151.501, 644.006
Charon raw centroid	216.488, 406.532	155.388, 549.357	153.349, 549.643	156.476, 635.283	154.721, 635.494
Distortion correction	0.606, −0.033	0.611, --0.410	0.609, −0.407	0.316, −0.408	0.310, −0.400
Overlap correction	0.014, −0.067	0.003, --0.008	0.003, −0.008	--0.014, 0.037	−0.014, 0.037
Charon net observable	215.868, 406.632	)54.774, 549.775	152.737, 550.058	156.174, 635.654	154.425, 635.857
Star raw centroid	529.161, 381.616	521.790, 363.280	521.171, 363.105	561.594, 330.693	561.328, 330.297
Distortion correction	−0.703, 0.068	−0.683, 0.151	--0.681, 0.152	--0.762, 0.228	−0.761, 0.230
Star net observable	529.864, 381,548	522.473, 363.129	521.852, 362.953	562.356, 330.465	562.089, 330.067

	PLUTO6A	PLUTO6B	PLUTO7A	PLUTO7B	PLUTO8A
Pluto raw centroid	199.578, 610.268	198.58), 611.048	123.623, 697.554	122.683, 698.549	706.686, 457.102
Distortion correction	0.465, −0.579	0.463, −0.577	--0.241, 0.112	--0.255, 0.126	−0.560, -0.180
Albedo correction	−0.063, −0.060	−0.062, −0.060	-0.044, -0.066	−0.044, −0.066	−0.055, −0.064
Pinto net observable	199.176, 610.907	198.180, 611.685	123.908, 697.508	122.982, 698.489	707.301, 457.346
Charon raw centroid	202.989, 602.184	202.068, 602.903	127,036, 690.381	126.282, 691.400	711.115, 450.984
Distortion correction	0.483, −0.584	0.482, -0.58'2	−0.168, 0.034	−0.180, 0.047	−0.539, −0.170
Overlap correction	−0.016, 0.038	−0.016, 0.038	--0.004, 0.008	−0.004, 0.008	0.003, −0.005
Charon net observable	202.522, 602.730	201.602, 603.447	127.208, 690.33{1	126.466, 691.345	711.651, 451.159
Star raw centroid	642.336, 178.954	642.727, 178.598	(,14.596, 116.653	614.959,)16.938	137.028, 551.973
Distortion correction	−0.337, 0.051	−0.336, 0.049	−0.251, 0.029	−0.251, 0.028	0.588, -0.373
Star net observable	642.673, 178.903	643.063, 178.549	614.847, 116.624	615.210, 116.910	136.440, 552.346

	PLUTO8B	PLUTO9A	PLUTO9B	PLUTO10A	PLUTO10B
Pluto raw centroid	704.963, 457.196	677.146, 236.905	675.377, 237.306	580.217, 525.885	578.645 , 526.135
Distortion correction	−0.569, −0.182	−0.351, 0.000	−0.359, 0.006	−0.625, −0.433	−0.622, −0.435
Albedo correction	—0.055, —0.064	−0.050, −0.046	−0.050, --0.046	−0.053, --0.030	−0.053, −0.030
Pluto net observable	705.587, 457,442	677.547, 236.951	675.786, 237.346	580.895, 526.348	579.320, 526.600
Charon raw centroid	709.326, 451.106	680.350, 232.371	678.628, 232.703	580.318, 529.878	578.710, 530.155
Distortion correction	−0.550, −0.172	−0.328, −0.016	−0.336, −0.009	−0.615, −0.439	−0.612, −0.441
Overlap correction	0.003, −0.005	0.051, -0.072	0.05), --0.072	0.000, −0.010	O.OOO, −0.010
Charon net observable	709.873, 451.283	680.627, 232.459	678.913, 232.784	580.933, 530.327	579.322, 530.606
Star raw centroid	137.009, 551.955	185.585, 308.359	185.560, 308.355	284.632, 304.262	284.637, 304.256
Distortion correction	0.588, −0.373	0.695, 0.309	0.694, 0.309	0.503, 0.438	0.503, 0.438
Star net observable	136.421, 552.328	184.890, 308.050	184.866, 308.046	284.129, 303.824	284.134, 303.818

TABLE 2 (continued)

	PLUTO11A	PLUTO11B	PLUTO12A	PLUTO12B	PLUTO13A
Pluto raw centroid	531.748, 606.296	530.330, 606.529	472.167, 713.765	470.670, 714.111	259.523, 739.332
Distortion correction	−0.381, −0.524	−0.379, −0.526	−0.160, −0.343	−0.159, −0.345	−0.019, −0.241
Albedo correction	−0.056, −0.034	−0.056, −0.034	−0.058, −0.039	−0.058, −0.039	−0.056, −0.041
Pluto net observable	532.185, 606.854	530.765, 607.089	472.385, 714.147	470.887, 714.495	259.598, 739.614
Charon raw centroid	530.083, 613.445	528.482, 613.854	468.650, 722.230	467.139, 722.508	255.874, 747.306
Distortion correction	−0.364, −0.519	−0.362, −0.521	−0.149, −0.306	−0.149, −0.309	−0.057, −0.157
Overlap correction	−0.004, 0.018	−0.005, 0.018	0.018, −0.042	0.018, −0.042	0.016, −0.036
Charon net observable	530.451, 613.946	528.849, 614.357	468.781, 722.578	467.270, 722.859	255.915, 747.499
Star raw centroid	327.322, 233.445	327.331, 233.446	378.225, 145.536	378.224, 145.550	208.571, 91.128
Distortion correction	0.282, 0.822	0,282, 0,822	−0.052, 0.806	−0.052, 0.806	0.232, 0.568
Star net observable	327.040, 232.623	327.049, 232.624	378.277, 144.730	378.276, 144.744	208.339, 90.560

	PLUTO13B	PLUTO14A	PLUTO14B
Pluto raw centroid	258.062, 739.641	518.840, 733.492	517.615, 734.357
Distortion correction	−0.021, −0.233	−0.086, −0.081	−0.086, −0.080
Albedo correction	−0.056, −0.041	−0.055, −0.041	−0.055, −0.041
Pluto net observable	258.139, 739.915	518.981, 733.614	517.756, 734.478
Charon raw centroid	254.354, 747.607	517.967, 741.605	516.726, 742.463
Distortion correction	−0.060, −0.149	−0.068, −0.029	−0.068, −0.027
Overlap correction	0.017, −0.036	0.002, −0.017	0.002, −0.017
Charon net observable	254.397, 747.792	518.033, 741.651	516.792, 742.507
Star raw centroid	208.566, 91.117	246.732, 78.842	246.741, 78.869
Distortion correction	0.232, 0.568	0.145, 0.545	0.145, 0.545
Star net observable	208.334, 90.549	246.587, 78.297	246.596, 78.324

TABLE 3. Coefficients of the adopted field distortion model. The a_{ij} and b_{ij} are measured in pixels. Uncertainties, in parentheses, are standard errors expressed in units of the fourth decimal.

ij	a_{ij}		b_{ij}		ij	a_{ij}		b_{ij}		ij	a_{ij}		b_{ij}	
01	0.0000	–	0.0176	(49)	26	−0.0181	(128)	−0.1796	(131)	53	−0.0838	(222)	−0.0425	(229)
02	−0.0008	(36)	0.0431	(35)	27	0.0214	(139)	0.0672	(141)	54	0.0410	(219)	0.0892	(224)
03	0.0047	(45)	0.8860	(46)	30	0.8952	(44)	0.0107	(45)	55	0.1944	(238)	−0.1319	(245)
04	−0.0722	(44)	−0.0483	(45)	31	−0.0343	(112)	−0.1397	(116)	56	−0.0121	(195)	−0.0022	(199)
05	−0.0083	(50)	0.0374	(51)	32	−0.0010	(150)	−0.0219	(154)	57	−0.1049	(206)	0.0265	(210)
06	0.0537	(39)	−0.0144	(40)	33	0.0796	(198)	0.1100	(203)	60	0.0431	(41)	0.0143	(42)
07	0.0009	(42)	−0.0225	(43)	34	−0.0172	(191)	−0.1218	(194)	61	0.0043	(101)	−0.0182	(103)
10	0.0000	–	−0.1020	(49)	35	0.0069	(208)	0.1196	(213)	62	0.0831	(139)	0.0640	(142)
11	0.1912	(66)	0.3482	(70)	36	0.0496	(166)	0.0731	(168)	63	0.0748	(181)	−0.0006	(185)
12	1.4785	(85)	−0.0501	(87)	37	0.0981	(177)	− 0.1080	(180)	64	−0.0990	(184)	0.0626	(187)
13	−0.0132	(113)	−0.0679	(116)	40	−0.0376	(45)	0.0046	(46)	65	−0.0691	(199)	0.0543	(202)
14	0.0860	(107)	0.0266	(109)	41	0.0610	(112)	0.0196	(115)	66	0.0176	(174)	−0.0559	(176)
15	−0.1065	(120)	−0.0606	023)	42	−0.0153	(152)	−0.0326	(155)	67	−0.0692	(177)	0.0087	(180)
16	0.0104	(93)	0.0159	(95)	43	0.0277	(199)	−0.0716	(204)	70	−0.0038	(43)	−0.0017	(44)
17	0.1299	(101)	0.0980	(103)	44	0.1086	(197)	0.1582	(200)	71	−0.0090	(103)	−0.0073	(106)
20	0.1614	(34)	−0.0635	(36)	45	0.0454	(213)	−0.1500	(218)	72	−0.0222	(144)	−0.0001	(147)
21	0.0104	(86)	1.4946	(88)	46	−0.1636	(177)	0.2314	(179)	73	0.0617	(183)	0.0338	(188)
22	−0.0309	(112)	−0.0021	(,115)	47	0.0118	(183)	−0.0993	(186)	74	0.0577	(188)	−0.0621	(192)
23	0.0217	(153)	0.0526	(157)	50	−0.0043	(51)	0.0115	(52)	75	−0.0121	(204)	0.0735	(208)
24	−0.0127	(144)	−0.0656	(147)	51	0.0038	(126)	0.0891	(130)	76	0.0072	(173)	0.0189	(175)
25	0.0554	(163)	0.1578	(168)	52	0.0339	(172)	0.0589	(177)	77	−0.0564	(181)	0.0659	084)

TABLE 4. Centroid shifts due to the finite disk of Pluto, obtained for each visit using the programs COMP and TINYTIM.

Visit	COMP	TINYTIM
1	–0.032, –0.032	–0.008, –0.016
2	–0.034, –0.036	–0.007, –0.019
3	–0.026, -0.033	–0.005, –0.035
4	0.013, 0.020	–0.005, –0.032
5	–0.009, –0.020	–0.010, –0.033
6	0.018, 0.015	–0.008, –0.032
7	–0,017, –0.012	–0.008, –0,035
8	–0.059, –0.048	–0.051, –0.040
9	–0.051, –0.040	--0.045, –0.051
10	–0.078, –0.041	–0.043, –0.035
11	–0.069, –0.039	-0.040, –0,036
12	–0.026, –0.010	–0.034, –0.037
13	0.061, –0.026	--0.030, –0.053
14	–0.084, –0.029	--0.037, –0.033
mean	–0.028, –0.024	--0.024, –0.036
s.e.	0.040, 0.020	0.017, 0.011
rms	0.048, 0.031	0.029, 0.037

TABLE 5. Centroid shifts for Charon due to image overlap with }'lute, binned by the separation between the two images.

Bin Center (pixels)	$\langle s \rangle$	σ_S	$\sigma_{S\Delta P}$	N	(s) $\langle S\rangle_{\rm Paper}$
3.9	−0.018	0.157	0.184	141	0.000
4.5	0.063	0.091	0.116	515	0.016
5.5	0.089	0.066	0.091	707	−0.014
6.5	0.062	0.071	0.079	865	−0.040
7.5	0.009	0.081	().081	978	-0.052
8.5	−0.037	0.068	0.078	1208	-0.046
9.5	−0.051	0.074	().086	1114	-0.020

TABLE 6. The adopted standard error for images of Pluto, Charon, and the reference stars.

Error Source	Pluto	Charon	Star
Raw centroid error	0.016	0.053	0.016
Field distortion	0.006	0.006	0.006
Field distortion contingency	0.020	0.020	0.020
Albedo variations	0.030	0.000	0.000
Pluto uniform disk	0.036	0.000	0.000
Pluto Charon image overlap	0.000	– [a]	0.000
RSS per visit	0.054	0.057[b]	0.026
RSS per exposure	0.076	0.081[b]	0.037

Notes to TABLE 6

[a] Image overlap error for Charon was computed individually for each exposure. The resulting s.e. is the RSS of the image overlap se. and the s.e.'s for the other error sources.

[b] Excluding the contribution from Pluto-Charon image overlap.

TABLE 7. The adopted solution from this paper compared to solutions using only 1991 or 1993 data and to the solution presented in Paper 1. Uncertainties, in parentheses, are in units of the final digit for each parameter.

Parameter	Adopted Soln.	1991 data only	1993 data only	Paper 1
Charon/Pluto mass ratio, q	0.1237 (81)	0.1158 (227)	0.1204 (319)	0.0837 (137)
Charon semimajor axis, a (km)	19662 (81)	19504 (107)	19814 (120)	19405 (86)
eccentricity, e	0.0072 (67)			
long. of periapsis, ω (deg)	2 (35)			—
mean longitude, λ (deg)	123.58 (43)	12340 (50)	123.69 (53)	123.01 (24)
inclination, i (deg)	96.57 (24)	96.58 (33)	96.56 (34)	96.56 (26)
Scale in 1991 ("/pixel)	0.10148 (1)	0.10147 (3)		0.10142 (2)
Scale in 1993 ("/pixel)	0.10)50 (1)		0.10151 (3)	

TABLE 8. The adopted solution from this paper compared to solutions by Young *et al.* (1994) and Tholen & Buie (1990). Uncertainties, in parentheses, are in units of the final digit for each parameter.

Parameter	This Paper		Y94		TB90	
Charon/Pluto mass ratio, q	0.1237	(81)	0.11566	(35)		
Charon semimajor axis, a (km)	19662	(81)	19460	(58)	19640	(320)
eccentricity, e	0.0072	(67)			0.0002	(2)
mean longitude, λ (deg)	123.58	(43)	122.77[a]	(20)	122.77	(20)
inclination, i (deg)	96.57	(24)	95.00	(24)	99.10	(100)

Note to TABLE 8

[a] Not solved for, hut copied from Tholen & Buie (1990).

TABLE 9. Postfit residuals, in pixels, and weighted postfit residuals for images of }']u1o, Charon, and the reference stars. The adopted standard error for Charon images is also tabulated; the standard error for all images of Pluto and the reference stars was 0.076 and 0.037 pixel, respectively, as shown in TABLE 6.

Exposure	Pluto Residual	Pluto wt. Res.	Charon Residual	Charon Std. Error	Charon Wt. Res.	Star Residual	Star Wt. Res.
PLUTO1A	0.004, 0.020	0.0, 0.3	–0.025, –0.133	0.137, 0.134	-0,2, --1.0	0.001, 0.005	0.0, 0.1
PLUTO1B	0.022, 0.003	0.3, 0.0	–0.076, –0.025	0.137, 0.134	- 0.6, --0.2	0.000, 0.001	0.0, 0.0
PLUTO2A	–0.005, –0.015	–0.1, –0.2	–0.003, –0,009	0.140, 0.131	0.0, --0,1	0.002, 0.004	0.0, 0.1
PLUTO2B	0.029, 0.054	0.4, 0.7	–0.033, –0.003	0.139, 0.131	- 0.2, 0.0	–0.004, –0.013	–0.1, –0.3
PLUTO3A	–0.015, 0.022	-0.2, 0.3	–0.040, –0.076	0.175, 0.147	- 0.2, --0.5	0,005, 0.000	0.1, 0.0
PLUTO3B	–0.016, 0.014	–0.2, 0.2	–0.090, –0.043	0.175, 0.147	- 0.5, --0.3	0.008, –0.001	0.2, 0.0
PLUT'04A	0.003, –0.010	0.0, –0.1	0.043, 0.005	0.140, 0.140	0.3, 0.0	–0.004, 0.002	–0.1, 0.1
PLUTO4B	0.033, –0.002	0.4, 0.0	0.028, –0.067	0.140, 0.140	0.2, --0.5	–0.010, 0.005	–0.3, 0.1
PLUTO5A	0.048, –0.032	0.6, –0.4	0.015, –0.025	0.137, 0.128	0.1, --0.2	–0.013, 0.010	–0.3, 0.3
PLUTO5B	0.031, –0.005	0.4, –0.1	–0.095, 0.007	0.137, 0.128	-0.7, 0.1	0.000, 0.000	0,0, 0.0
PLUTO6A	--0.037, 0.026	--0.5, 0.3	–0.123, 0,132	0,138, 0.130	- 0.9, 1.0	0.018, –0.017	0.5, --0.5
PLUTO6B	0.003, –0.010	0.0, –0.1	–0,011, 0.030	0.138, 0.130	- 0.1, 0.2	0.000, 0.000	0.0, 0.0
PLUTO7A	0.047, –0.034	0.6, –0.4	–0.075, 0.015	0.138, 0.135	- 0.5, 0.1	–0.006, 0.007	–0.2, 0.2
PLUTO7B	–0.026, –0.001	--0.3, 0.0	0.040, 0.056	0.138, 0.135	0.3, 0.4	0.003, –0.004	0.1, -0.1
PLUTO8A	–0.058, 0.021	--0.8, 0.3	–0.006, –0.036	0.140, 0.140	0.0, --0.3	0.014, –0.002	0.4, --0.1
PLUTO8B	0.004, 0.011	0.1, 0.1	–0.003, –0.039	0.140, 0.140	0,0, --0.3	–0.001, 0.000	0.0, 0.0
PLUTO9A	0.054, –0.010	0.7, –0.1	–0.042, 0.012	0.143, 0.134	- 0.3, 0.1	–0,010, 0.001	–0.3, 0.0
PLUTO9B	0.027, 0.017	0.4, 0.2	–0.015, –0.061	0.143, 0.134	- 0.1, --0.5	–0.005, 0.001	–0.1, 0.0
PLUTO10A	0.001, 0.008	0.0, 0.1	0.062, –0.028	0.263, 0.227	0.2, --0.1	–0.002, –0.001	0.0, 0.0
1'LU'1'O1OB	–0.006, 0.002	--0.1, 0.0	0.034, –0.038	0.263, 0.227	0.1, --0.2	0.001, 0.00)	0.0, 0.0
PLUTO11A	-0.043, 0.008	--0.6, 0.1	0.110, –0.086	0.140, 0.138	0.8, –0.6	0.002, 0.004	0.1, 0.1
PLUTO11B	–0.006, –0.034	--0.1, –0.4	–0.025, 0.030	0.140, 0.138	- 0.2, 0.2	0.003, 0.006	0.1, 0.2
PLUTO12A	0.036, 0.017	0.5, 0.2	–0.096, 0.081	0.141, 0.132	-0.7, 0.6	–0.002, –0.011	0.0, –0.3
PLUTO12B	0.035, 0.020	0.5, 0.3	–0.104, 0.020	0.111, 0.132	- 0.7, 0.2	–0.001, –0.006	0.0, –0.2
PLUTO13A	-0.007, 0.008	-0.1, 0.1	0.029, 0.046	0.136, 0.129	0.2, 0.4	0.000, –0.006	0.0, –0.2
PLUTO13B	0.003, –0.028	0.0, –0.4	–0.016, 0.014	0.136, 0.129	- 0.1, 0.1	0.000, 0.005	0,0, 0.1
PLUTO14A	–0.002, –0.019	0.0, –0.3	–0.001, 0.045	0.138, 0.132	0.0, 0.3	0.000, 0.001	0.0, 0.0
PLUTO14B	–0.008, –0.042	--0.1, –0.6	–0.017, 0.032	0.138, 0.132	- 0,1, 0.2	0.003, 0.007	0.1, 0.2
mean	0.005, 0.000	0.1, 0.1	–0.019, –0.005		- 0.1, 0.0	0.000, 0.000	0.0, 0.0
sigma	0.028, 0.022	0.4, 0.3	0.055, 0.055		0.4, 0.4	0.006, 0.006	0.2, 0.2

TABLE 10. Predicted separation in pixels between images of Pluto and the reference star in each exposure, with postfit residuals and weighted postfit residuals for the same. The standard error in the separation was 0.085 pixel for each exposure.

Exposure	Sep.	Resid.	wt. Res.
PLUTO1A	545.681	–0.015	--0.2
PLUTO1B	545.342	–0.005	--0.1
PLUTO2A	431.155	0.020	0.2
PLUTO2B	431.001	–0.074	--0.9
PLUTO3A	314.784	0.023	0.3
PLUTO3B	316.227	0.025	0.3
PLUTO4A	417.716	–0.012	--0.1
PLUTO4B	419.199	–0.041	--0.5
PLUTO5A	515.380	–0.074	--0.9
PLUTO5B	516.856	–0.028	--0.3
PLUTO6A	619.126	0.069	0.8
PLUTO6B	620.908	–0.008	--0.1
PLUTO7A	760.557	–0.065	--0.8
PLUTO7B	761.920	0.021	0.3
PLUTO8A	578.712	–0.075	--0.9
PLUTO8B	577.021	0.003	0.0
PLUTO9A	497.761	0,064	0.8
PLUTO9B	495.985	0,030	0.4
PLUTO10A	370.927	0.008	0.1
PLUTO10B	369.819	–0.005	--0.1
PLUTO11A	426.771	–0.01/3	--0.2
PLUTO11B	426.291	–0.039	.–0.5
PLUTO12A	577.142	0.034	0.4
PLUTO12B	577.229	0.031	0.4
PLUTO13A	651.075	0.013	0.2
PLUTO13B	651.273	–0.033	–0.4
PLUTO14A	709.675	–0.020	-0,2
PLUTO14B	709.976	–0.050	–0.6
mean		–0.008	–0.1
sigma		0.039	0.5

TABLE 11. Sensitivity of the mass ratio q to changes in the various calibration models. The rightmost column gives the RSS residual of the separation between images of Pluto and the reference star.

Case	'91 only q	'93 Only q	'91-'93 q	'91-'93 $\Delta q/\sigma_q$	'91-'93 σ_S
Adopted solution (Table 7)	**0.116**	0.120	0.124	**0.00**	0.039
No scale-difference *a priori*	0.116	0.120	0.118	−0.74	0.039
No distortion model	0.134	0.034	0.091	−4.07	0.253
3 x 3 distortion model	0.064	0.163	0.128	0.49	0.110
5 x 5 distortion model	0.086	0.149	0.119	−0.62	0.059
6 x 6 distortion model	0.112	0.141	0.121	−0.37	0.047
8 x 8 distortion model	0.119	0.113	0.125	0.12	0.041
9 x 9 distortion model	0.120	0.115	0.124	0.00	0.039
Paper I 6 x 6 distortion model	0.085	0.144	0.118	−0.74	0.071
METRIC 6 x 6 distortion model	0.111	0.109	0.131	0.86	0.057
COMP Pluto uniform disk	0.121	0.139	0.126	0.25	0.036
TINYTIM Pluto uniform disk	0.117	0.123	0.124	0.00	0.039
Remove albedo correction	0.124	0.122	0.122	−0.25	0.039

TABLE 12. Sensitivity of Charon's orbital elements to changes in the various calibration models, expressed as fractions of the formal error of the adopted solution.

Calibration Change	$\Delta a/\sigma_a$	$\Delta i/\sigma_i$	At/o.
Remove albedo correction	–0,1	–0.4	0.1
Remove image overlap correction	–0.2	-0.1	–0.1
Use Paper 1 overlap correction	–1.2	0.0	0.0
Remove scale-difference *a* priori	**0.0**	**0.0**	**0.(1**

TABLE 13. Sensitivity of Charon's orbital elements 10 a *priori* constraints on them. Uncertainties, in parentheses, arc in units of the final digit for each parameter.

Parameter	Adopted Solution	Perfect eccentricity	Remove node a *priori*	No a priori
Semimajor axis, a (km)	19662 (81)	19664 (79)	19657 (81)	19652 (81)
Eccentricity, e	0.0072 (67)		0.0073 (67)	0.0126 (75)
Long. of periapsis, w (deg)	2 (35)		2 (35)	1 (20)
Inclination, i (deg)	96.57 (24)	96.54 (23)	96.59 (24)	96.58 (24)
R. A. of asc. node, Ω (deg)	from TB90	from TB90	221.810 (430)	222.780 (430)
Mean longitude, λ (deg)	123.58 (43)	123.46 (41)	123.34 (62)	127.39 (279)
Period, P (deg/day)	from TB90	from TB90	from TB90	6.387452 (138)

TABLE 14. Masses and gravitational constants derived from the solution parameters in TABLE ?. uncertainties, in parentheses, are in units of the final digit for each parameter.

Parameter	Solution
Mass of Pluto system, $\mathcal{M}_{sys}$ (10^{24} g)	14.76 (18)
Mass of Pluto, $\mathcal{M}_{P}$ (10^{24} g)	13.14 (18)
Mass of Charon, $\mathcal{M}_{C}$ (10^{24} g)	1.62 (9)
$G\mathcal{M}_{sys}$ (km^3/s^2)	985 (12)
$G\mathcal{M}_{P}$ (km^3/s^2)	877 (12)
$G\mathcal{M}_{C}$ (km^3/s^2)	108 (6)

TABLE 15. Computed densities of Pluto and Charon based on the masses from TABLE 14 and radii from the literature. Uncertainties, in parentheses, are in units of the final digit for each parameter.

Solution	Data Source	R_P (km)	R_C (km)	ρ_P (g/cm^3)	ρ_C (g/cm^3)
TB90	Mutual events	1151[a] (6)	593" (13)	2.05 (3)	1.85 (16)
YB94	Mutual events	1176[a] (6)	628[a] (16)	1.92 (3)	1.56 (15)
EY92 "haze"	Pluto stellar occultation	< 1181		>1.90	--
EY92 '(thermal gradient"	Pluto stellar occultation	1206 (11)		1.79 (5)	–
EY91	Charon stellar occultation	· ·	>601.5		< 1.78
A94-F550M	*HST* FOC images	1160	650	2.01	1.41
A94-F342W	*HST* FOC images	1160	635	2.01	1.52

Note to TABLE]5

[a] These values, denoted $\hat{R}_P$ and $\hat{R}_C$ in Sec. 6, presume $a = 19640$ km; our solution for a implies R_P = 1152 ± 8 km and R_C = 594413 km for TB90, and R_P = 1177 ± 8 km and R_C = 629:1 13 km for YB94.

Figure 1

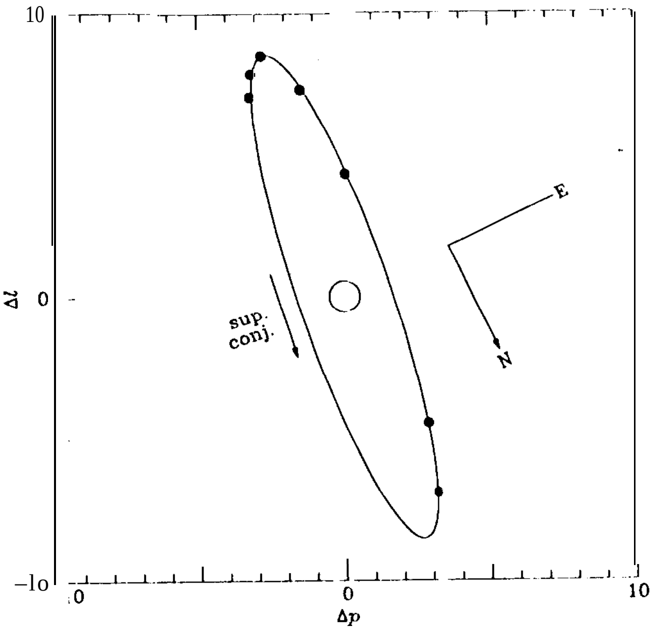

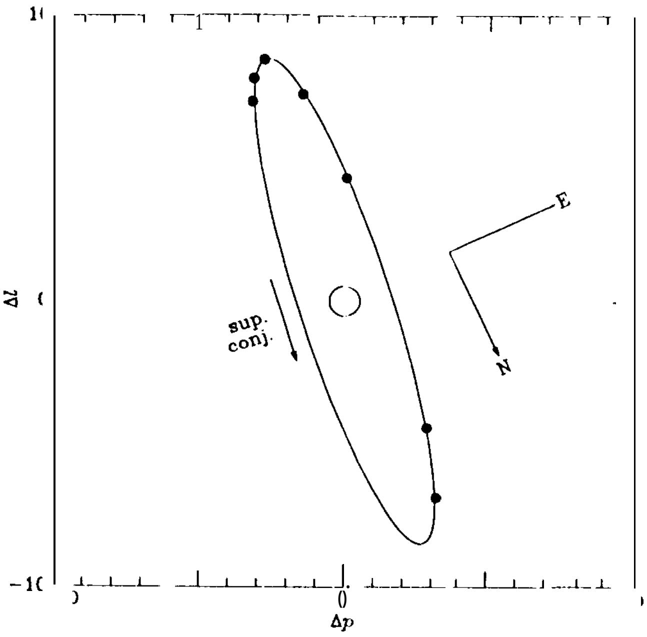

sup.
conj.
E
N
Δl
Δp

Figure 2

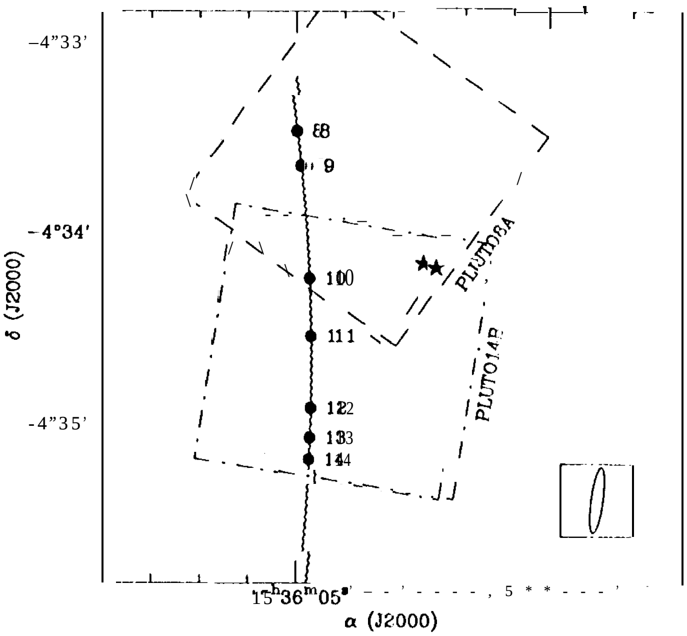

−4°33′
−4°34′
−4°35′
δ (J2000)
8
9
10
11
12
13
14
PLUTO8A
PLUTO14B
15h36m05s
α (J2000)

Figure 3

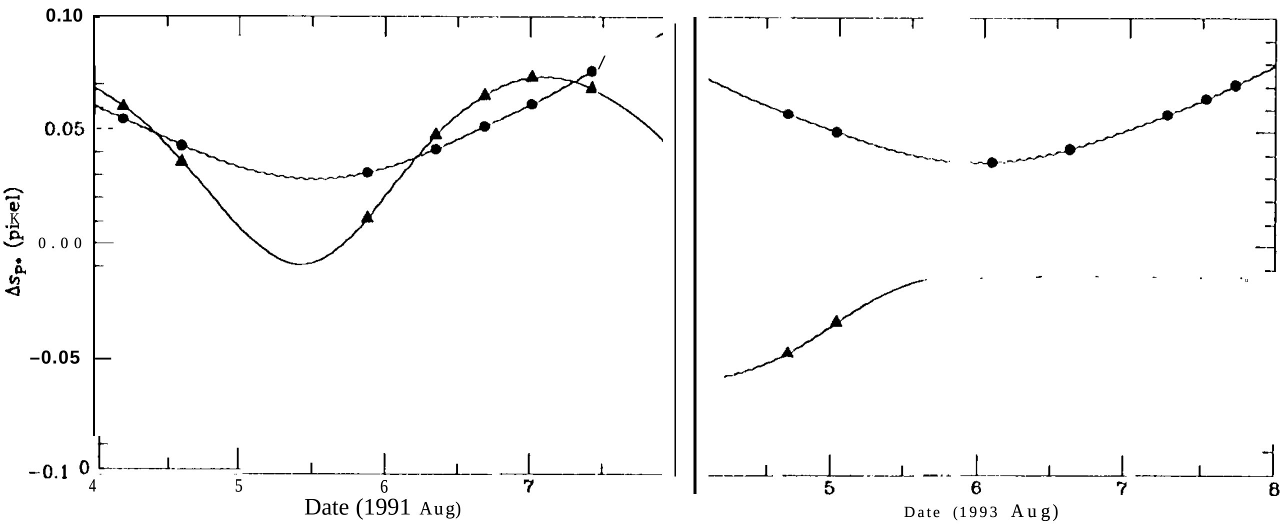
0.10
0.05
0.00
−0.05
−0.10
Δs_{p*} (pixel)
4
5
6
7
Date (1991 Aug)
5
6
7
8
Date (1993 Aug)

Figure 4

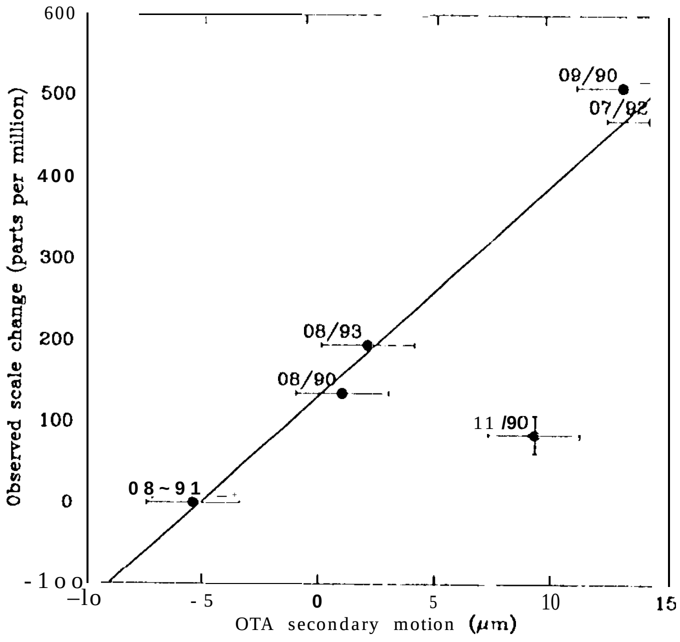

600
500
400
300
200
100
0
-100
Observed scale change (parts per million)
09/90
07/92
08/93
08/90
11/90
08~91
-10
-5
0
5
10
15
OTA secondary motion (μm)